Supplemental material to this article can be found at:
http://dmd.aspetjournals.org/content/suppl/2019/07/29/dmd.119.087023.DC1

1521-009X/47/10/1146–1155$35.00
DRUG METABOLISM AND DISPOSITION
Copyright © 2019 by The American Society for Pharmacology and Experimental Therapeutics
https://doi.org/10.1124/dmd.119.087023
Drug Metab Dispos 47:1146–1155, October 2019

DRUG METABOLISM & DISPOSITION

Special Section on Pharmacokinetic and Drug Metabolism Properties of Novel Therapeutic Modalities

Exposure-Efficacy Analysis of Antibody-Drug Conjugates Delivering an Excessive Level of Payload to Tissues

Donglu Zhang, Peter S. Dragovich, Shang-Fan Yu, Yong Ma, Thomas H. Pillow, Jack D. Sadowsky, Dian Su, Wei Wang, Andrew Polson, S. Cyrus Khojasteh, and Cornelis E.C.A. Hop[1]

Drug Metabolism & Pharmacokinetics (D.Z., Y.M., D.S., W.W., S.C.K., C.E.C.A.H.), Discovery Chemistry (P.S.D., T.H.P.), Translational Oncology (S.-F.Y., A.P.), and Protein Chemistry (J.D.S.), Genentech, South San Francisco, California

Received March 3, 2019; accepted July 26, 2019

ABSTRACT

Antibody-drug conjugates (ADCs) contain a disease-receptor antibody and a payload drug connected via a linker. The payload delivery depends on both tumor properties and ADC characteristics. In this study, we used different linkers, attachment sites, and doses to modulate payload delivery of several ADCs bearing maytansinoids (e.g., DM1), auristatins (e.g., MMAE), and DNA alkylating agents [e.g., pyrrolo[2,1-c][1,4]benzodiazepine-dimer (PBD)] as payloads in HER2- or CD22-expressing xenograft models. The tumor growth inhibition and ADC stability and exposure data were collected and analyzed from these dosed animals. The trend analysis suggests that intratumoral payload exposures that directly related the combination of conjugate linker and dose correlate with the corresponding efficacies of three payload types in two antigen-expressing xenograft models. These preliminary correlations also suggest that a minimal threshold concentration of intratumoral payload is required to support sustained efficacy. In addition, an ADC can deliver an excessive level of payload to tumors that does not enhance efficacy ("Plateau" effect). In contrast to tumor payload concentrations, the assessments of systemic exposures of total antibody (Tab) as well as the linker, dose, site of attachment, plasma stability, and drug-to-antibody ratio changes of these ADCs did not consistently rationalize the observed ADC efficacies. The requirement of a threshold payload concentration for efficacy is further supported by dose fractionation studies with DM1-, MMAE-, and PBD-containing ADCs, which demonstrated that single-dose regimens showed better efficacies than fractionated dosing. Overall, this study demonstrates that 1) the linker and dose together determine the tissue payload concentration that correlates with the antitumor efficacy of ADCs and 2) an ADC can deliver an unnecessary level of payload to tumors in xenograft models.

Introduction

Antibody-drug conjugates (ADCs) have become an important drug-delivery technology for targeted therapies. ADC payloads (drugs) are often potent antimitotic cytotoxins such as the maytansinoid present in ado-trastuzumab emtansine (KADCYLA, T-DM1) and the auristatin contained in brentuximab vedotin (Adcetris, MMAE) and polatuzumab vedotin (Polivy, MMAE), as well a DNA-alkylating agent calicheamicin-derivative in inotuzumab ozogamicin (BESPONSA) (Doronina et al., 2003; LoRusso et al., 2011; Ricart, 2011; Shor et al., 2015; Beck et al., 2017). More recently, other potent DNA alkylating agents such as pyrrolo[2,1-c][1,4]benzodiazepine-dimers (PBDs) have also been employed as ADC payloads (Antonow and Thurston, 2011; Jeffrey et al., 2013). An ADC undergoes antigen binding, tissue uptake, cell internalization, and biochemical transformation (proteolytic degradation of antibody, linker cleavage, and immolation) to release its payload. The plasma pharmacokinetic profile of an ADC is determined by the antibody and is characterized by low clearance, small volume of distribution, long circulating half-life (days), and target or nontarget tissue distribution. Consequently, ADCs modify drug disposition and enable slow payload release in targeted tissues. The rate and extent of payload delivery depends on both tumor properties (such as antigen type, antigen expression and turnover rate, and tumor type) and ADC structural characteristics. The level of payload in the tumor is determined by the amount of conjugate entering the tissue, the local ADC catabolism rate, and payload tissue-retention properties.

Multiple payload (drug) molecules can be conjugated to an antibody through linkers and the ratio is defined as drug-to-antibody ratio (DAR).

[1]Current affiliation: Genentech, 1 DNA Way, South San Francisco, CA 94080. E-mail: hop.cornelis@gene.com
https://doi.org/10.1124/dmd.119.087023.
This article has supplemental material available at dmd.aspetjournals.org.

ABBREVIATIONS: ADC, antibody-drug conjugate; AUC, area under amount or concentration-versus-time curve; CI, confidence intervals; DAR, drug-to-antibody ratio; DMx, maytansinoid DM1, DM3, or DM4; i.v., intravenous(ly); LC, liquid chromatography; MCC, maleimidomethyl cyclohexane-1-carboxylate; MMAE, monomethyl auristatin E; MMTV-HER2, murine mammary tumor virus promoter; MRM, multiple reaction monitoring; MS, mass spectrometry; MS/MS, tandem mass spectrometry; PBD, pyrrolo[2,1-c][1,4]benzodiazepine-dimer; Tab, total antibody (could include DAR2, DAR1 and DAR0 species for ADCs in this study); TGI, relative tumor growth inhibition; TGI_{rel}, relative tumor growth inhibition.

Downloaded from dmd.aspetjournals.org at ASPET Journals on April 18, 2024

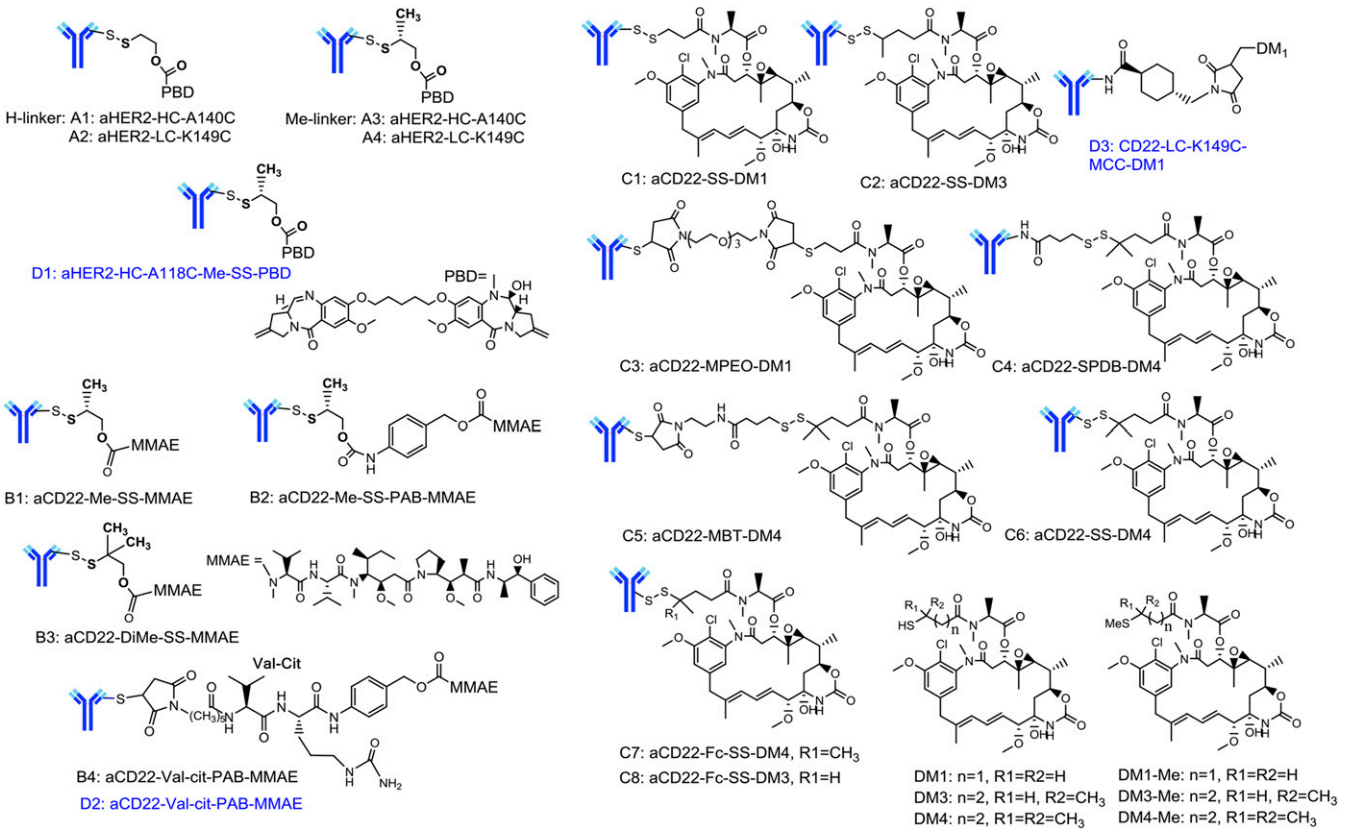

Fig. 1. Chemical structures of antibody-drug conjugates and payloads or catabolites used in this study.

The DAR value is approximately 3.5 for Kadcyla and Adcetris (Wei et al., 2018). The common cleavable linkers that are used to connect payloads to antibodies include the dipeptide linker via maleimide addition to cysteine thiol or a disulfide linking to cysteine thiol in antibodies. Deconjugation could occur through reverse-Michael addition of the maleimide connection or disulfide cleavage in circulation (Su et al., 2018; Zhang et al., 2019). Following administration to animals or humans of an ADC with DAR = 2, antibody species of DAR0, DAR1, DAR2 could be present in circulation. Therefore, the stability of an ADC could be measured by following the change in DAR values, which could affect efficacy of an ADC (Wei et al., 2018).

Anti-CD22-linked PBD conjugates containing a cyclobutyl-substituted disulfide linker were reported to exhibit strong efficacy in a WSU-DLCL2 xenograft mouse model whereas an ADC derived from a closely-related cyclopropyl linker was inactive (Ma et al., 2016; Zhang et al., 2016a,b). Although ADC exposures and the DAR values of the two ADCs were similar in circulation, the former ADC efficiently released its PBD payload in tumors but the latter only generated a nonimmolating thiol-containing catabolite that did not effectively bind to DNA. These results demonstrate that intratumoral catabolites can determine ADC in vivo efficacy, which may not easily be revealed via assessment of traditional systemic pharmacokinetic properties.

In this study, efficacy experiments were conducted in mouse xenograft models that employed conjugates containing the payloads commonly used in ADC designs (e.g., DM1, MMAE, and PBD) to understand if there is a quantitative correlation between the efficacy and ADC systemic exposures (represented by total antibody) and corresponding intratumoral payload exposures. These ADCs contain a variety of linkers (disulfide, peptide, noncleavable), have different conjugation sites, and display a spectrum of plasma stabilities. Tumor and plasma samples were collected during these experiments at different time points from selected animals to determine total antibody (Tab) concentrations and DAR in addition to payload concentrations in tissues. These parameters were subsequently correlated with observed tumor growth inhibition. In addition, dose-fractionation studies of selected ADCs containing disulfide, dipeptide, or MCC noncleavable linkers and PBD, MMAE, or DM1 as payloads were investigated to better understand the requirement of achieving and/or maintaining a threshold intratumoral payload concentration that would support sustained antitumoral efficacy.

Materials and Methods

Materials

Ammonium formate and formic acid were purchased from Sigma-Aldrich (St. Louis, MO). Human HER2 and CD22 antibodies with two engineered cysteine residues (THIOMAB antibodies) were generated at Genentech as described previously (Polson et al., 2010; Bhakta et al., 2013; Junutula and Gerber, 2016). Maytansinoids DM1, DM3, and DM4 and their methylated catabolites DM1-Me, DM3-Me, and DM4-Me were prepared as described previously (Widdison et al., 2015). Mice (CB-17 SCID, female, nude, and Balb/C strains) were purchased from Charles Rivers Laboratories (Mattawan, MI). All animal studies were carried out in compliance with National Institutes of Health guidelines for the care and use of laboratory animals and were approved by the Institutional Animal Care and Use Committee at Genentech, Inc.

Preparation of ADC Conjugates

Full length, cysteine-engineered monoclonal antibodies (THIOMAB antibodies) expressed in Chinese hamster ovary cells were prepared as described previously (Zhang et al., 2016a). Anti-HER2 conjugates on light chain K149C, heavy chain A140C of non-methyl- and methyl-disulfide–linked PBD-dimer (A1: aHER2-heavy chain-H-SS-PBD, A2:aHER2-LC-H-SS-PBD, A3:aHER2-heavy

Downloaded from dmd.aspetjournals.org at ASPET Journals on April 18, 2024

TABLE 1

The ADC structures, animal parameters, and systemic exposures in efficacy studies using ADCs containing PBD, MMAE, DM1, DM3, and DM4 as payloads ($n = 8$ for efficacy analysis and $n = 3$ for exposure analysis)

Conjugate	ADC Name	ADC Structures[a]			Animal Parameters			Systemic Exposure		Efficacy (Range, 95%CI)
		Linker	Payload	Attaching Site	Antigen	Animal Models	Intravenous Dose[b]	Tab (μg/ml)[c]	DAR at D10, 4, or 7[d]	AUC/day TGI_{rel} %[e]
A1	HER2-heavy chain-H-SS-PBD	H-Disulfide	PBD	Heavy chain A140C	HER2	Fo5	4	20.7/5.31/0.67	0.9	88 (37, 146)[f]
A2	HER2-light chain-H-SS-PBD	H-Disulfide		Light chain K149C			4	24.1/8.80/5.04	1.0	63 (18, 120)[f]
A3	HER2-heavy chain-Me-SS-PBD	Me-Disulfide		Heavy chain A140C			0.4	1.41/0.53/0.35	1.7	44 (1, 89)[f]
sA4	HER2-light chain-Me-SS-PBD	Me-Disulfide		Light chain K149C			0.4	1.42/0.33/0.02	1.6	114 (59, 190s)[f]
B1_1	CD22-Me-SS-MMAE	Me-Disulfide	MMAE	Light chain K149C	CD22	BJAB	1	17.3/12.8/15.8	1.8	ND
B1	CD22-Me-SS-MMAE	Me-Disulfide					20	229/313/232	1.8	50 (−58, 87)
B2	CD22-Me-SS-PAB-MMAE	Me-SS-PAB					20	193/141/176	1.8	129 (105, 186)
B3	CD22-DiMe-SS-MMAE	DiMe-Disulfide					20	135/123/115	1.7	69 (−16, 107)
B4	CD22-Val-Cit-PAB-MMAE	Peptide					1	10.8/6.00/6.30	1.8	130 (108, 204)
C1	CD22-SS-DM1	Disulfide	DM1	Light chain K149C	CD22	BJAB	50	13.4/15.5/11.2	NA	120 (104,158)
C2	CD22-SS-DM3	Disulfide	DM3	Light chain				11.7/14.4/11.7	NA	129 (112, 178)
C3	CD22-MPEO-DM1	MPEO	DM1	K149C				15.6/14.9/12.1	2.0	22 (−165, 77)
C4	CD22-SPDB-DM4	SPDB	DM4	Lysine				7.90/6.60/4.60	NA	68 (−7, 98)
C5	CD22-MBT-DM4	MBT	DM4	Light chain K149C				13.1/11.0/6.80	0	67 (−11, 98)
C6	CD22-SS-DM4	Disulfide	DM4	Light chain K149C				13.8/13.5/8.9	1.9	125 (110, 167)
C7	CD22-Fc-SS-DM4	Disulfide	DM4	Fc S400C				15.6/11.5/13.7	1.4	117 (100, 150)
C8	CD22-Fc-SS-DM3	Disulfide	DM3	Fc S400C				13.8/10.7/10.0	0	73 (−4, 99)

NA, not analyzed; ND, not detected.

Part of PBD data has been published (Zhang et al., 2018) and was included here for comparison.

[a]ADCs had DAR values of 1.9–2 with aggregation of <5% and free remaining linker payload of <5% that were prepared from THIOMAB antibody.

[b]Dose was in milligrams per kilogram for conjugates A1–A5 and B1–B4, and in micrograms per square meter for groups C1–C8.

[c]Plasma samples were collected at days 4, 10, and 18 for A1–A4, days 1, 4, and 7 for B1-B4 and days 1, 3, and 7 for C1–C8.

[d]DAR values were at days 10, 4, and 7, respectively, for conjugates A1–A4, B1–B4, and C1–C8, respectively. The payloads were either not detected for PBD and MMAE or not analyzed for DMx in plasma.

[e]Tumor growth inhibition was quantified on the basis of AUC/day extrapolated from tumor size–time profile (Fig. 2, D and H) (Yu et al., 2015). TGI_{rel} was calculated from comparison of tumor growth in AUC/day of each conjugate to that of vehicle control (for B1–B4 and C1–C8).

[f]The AUC/day values extrapolated from tumor size-time profile. TGI_{rel} was calculated from comparison of tumor growth in AUC/day of each treatment (for A1–A3) to that of the least-active entity A4 (Fig. 2A) as described in the supplemental data (Yu et al., 2015).

chain-Me-SS-PBD, and A4:aHER2-light chain-Me-SS-PBD) used in Groups A1–A4 were prepared as described previously (Zhang et al., 2016a, 2018). Anti-CD22 conjugates of disulfide and peptide-linked monomethyl auristatin E, MMAE (B1:aCD22-Me-SS-MMAE, B2:aCD22-Me-SS-PAB-MMAE, B3:aCD22-DiMe-SS-MMAE, and B4:aCD22-va-cit-PAB-MMAE) used in Groups B1–B4, variously linked maytansinoids DM1, DM3, and DM4 (C1:CD22-SS-DM1, C2:aCD22-SS-DM3, C3:aCD22-MPEO-DM1, C4: aCD22-SPDB-DM4, C5:aCD22-MBT-DM4, C6:aCD22-SS-DM4, C7: aCD22-Fc-SS-DM4, C8:aCD22-Fc-SS-DM3) used in Groups C1–C8, and aHER2-A118C-Me-SS-PBD (D1), aCD22-val-cit-PAB-MMAE (D2), and aCD22-LC-K149C-MCC-DM1 (D3) as well as the corresponding control conjugates were prepared at Genentech as described previously (Pillow et al., 2014; Sadowsky et al., 2017). The structures of these ADCs and associated names, structural elements, and doses are shown in Fig. 1 and Table 1. These ADC conjugates had DAR values of 1.9–2 with aggregation of <5% and free remaining linker drug of <5%.

In Vivo Xenograft Studies: Efficacy and Tissue Collection

The founder 5 (Fo5) mouse mammary tumor model was employed to evaluate the in vivo efficacy of anti-HER2 disulfide–linked PBD conjugates as described previously (Lewis Phillips et al., 2008; Pillow et al., 2014). The Fo5 model is a transgenic mouse model in which the human HER2 gene is overexpressed in mammary epithelium under transcriptional regulation of the murine mammary tumor virus promoter (MMTV-HER2) and leads to spontaneous development of tumors expressing human HER2. The mammary tumor of one of these founder animals (Fo5) has been propagated in subsequent generations of Friend leukemia virus B (FVB) mice by serial transplantation of tumor fragments (approx. 2 × 2 mm in size). Before being used for an efficacy study, the Fo5 tumor fragments were surgically transplanted into #2/3 mammary fat pad area of female nu/nu mice (Charles River Laboratories). Conjuates A1, A2, A3, and A4 as well as conjugate D1 were dosed in these Fo5 xenograft animals (Fig. 1; Table 1).

The efficacy of the anti-CD22 ADCs was investigated in a mouse xenograft model of CD22-expressing human BJAB.Luc (Genentech cell line repository) as described previously (Polson et al., 2010; Yu et al., 2015). To establish the subcutaneous xenograft model, the tumor cells (20 million cells in 0.2 ml of Hank's balanced salt solution) were inoculated subcutaneously into the flanks of female CB17 ICR SCID mice (Charles Rivers Laboratories). Conjuates B1-B4, B1-1, and C1-C8 as well as conjugates D2 and D3 were dosed in these BJAB.Luc xenograft animals (Fig. 1; Table 1).

When tumor size reached a desired volume, animals were divided into groups of 8–12 mice and given a single intravenous dose via the tail vein with ADC conjugates (day 0). Tumors and body weights of mice were measured one to two times a week throughout the study. Mice were promptly euthanized when body weight loss was >20% of their starting weight. All animals were euthanized before tumors reached 3000 mm^3 or showed signs of impending ulceration. Tumor volume was measured in two dimensions (length and width) using calipers and the tumor volume was calculated using the formula: tumor size (mm^3) = (longer measurement × shorter measurement^2) × 0.5. The tumor volumes were plotted as a mean tumor volume ± S.E.M. of each group over time. Tumor stasis was defined

Downloaded from dmd.aspetjournals.org at ASPET Journals on April 18, 2024

as no tumor size change from day 0. Tumor growth inhibition (TGI) was calculated as percentage of area under the tumor size-time curve (AUC) per day of each treatment group in relation to vehicle or the least-active group A4 in MMTV-HER2/Fo5 models. The relative tumor growth inhibition (TGI_{rel}) was calculated as follows: $\%TGI_{rel} = 100 \times (AUC_{treatment}/day/AUC_{vehicle\ or\ least\ active\ treatment}/day)$ (Pillow et al., 2014; Yu et al., 2015). Accordingly, $\%TGI_{rel}$ in comparison with group A4 was 22.8%, 44.7%, and 61.4% for groups A1, A2, and A3, respectively (Table 1). The confidence intervals (CI) for %TGI were determined, and the 2.5 and 97.5 percentiles of CIs were reported as the low and high values of the range.

Blood samples were collected and plasma samples were prepared from selected tumor-bearing mice ($n = 2$ to 3/time point) from the efficacy groups for analysis of total antibody concentration and DAR values. Plasma samples were collected at days 4, 10, and 18 for anti-HER2-PBD ADCs (A1–A4), days 1, 4, and 7 for anti-CD22-MMAE ADCs (B1–B4), and days 1, 3, and 7 for anti-CD22-maytansinoid DM1 (DMx) ADCs (C1–C8) (Table 1). To minimize stress that might influence animal health or tumor response, sample collection times were rotated between animals so each animal was only bled once. Tumor tissues from the same set of animals were collected at days 4, 10, and 18 for anti-HER2 PBD ADCs (A1–A4), day 4 for anti-CD22 MMAE ADCs (B1-1, B1–B4), and day 21 (termination of all treatment groups) for anti-CD22 DMx ADCs (C1–C8) (Table 1). The vehicle control animals in the Fo5 efficacy study were terminated at day 7 owing to rapid tumor growth and could not be used as controls for TGI calculations. The plasma and tumor tissue samples were kept frozen at −80°C until being analyzed.

Dose Fractionation Studies

The doses and dosing schedules are labeled in the figure showing the tumor growth inhibition results (Fig. 4). Mice bearing MMTV-Her2/Fo5 ($n = 8$ each treatment group) were dosed with a single 1-mg/kg i.v. dose and 0.3-mg/kg doses every week three times with anti-HER2-heavy chain A118C-Me-SS-PBD ADC (conjugate D1). Tumors and body weights of mice were measured one to two times a week throughout the 4-week study. For anti-CD22-val-cit-PAB-MMAE ADC (conjugate D2), mice bearing BJAB.Luc ($n = 9$ each treatment group) were dosed with a single 1.5-mg/kg i.v. dose, 0.5-mg/kg doses every week three times, a single 3 mg/kg i.v. dose, and 1-mg/kg doses every week three times. Tumors and body weights of mice were measured one to two times a week throughout the 9-week study. For anti-CD22-MCC-DM1 ADC (conjugate D3), mice bearing BJAB.Luc ($n = 10$ each treatment group) were dosed with a single 6-mg/kg i.v. dose, 3-mg/kg doses two times every other week, and 2 mg/kg every week three times, with a single 3 mg/kg i.v. dose, 1.5-mg/kg doses two times every other week, and 1 mg/kg every week three times, as well as with a single 1.5-mg/kg i.v. dose, 0.75-mg/kg doses every other week two times, and 0.5 mg/kg every week three times. Tumors and body weights of mice were measured one to two times a week throughout the 6-week study. Tumor volume was measured in two dimensions as described above. The tumor volumes were plotted as a mean tumor volume ± S.E.M. of each group over time.

Measurements of Total Antibody and DAR

Total antibody concentration was determined by the ELISA method as described previously (Kozak et al., 2013). Plasma samples were analyzed for total antibody (conjugated plus unconjugated antibody) concentrations in microtiter plates (384 wells) (Nunc, Rochester, NY) that were coated with human HER2 (Genentech, Inc.). The limit of quantitation was 3 ng/ml. The DAR value was determined as described previously (Xu et al., 2011). Briefly, an appropriate volume of mouse plasma was incubated at room temperature with the biotinylated HER2 or CD22 target antigen, which was coupled to the streptavidin paramagnetic beads (Invitrogen). The bead-captured ADC analytes were washed and deglycosylated at 37°C overnight. The resulting samples in 30% acetonitrile in water containing 1% formic acid were injected onto a Triple TOF 5600 mass spectrometer (AB Sciex) coupled with HPLC using a reversed-phase column. The compounds were eluted by a gradient of mobile phase A (water with 0.1% formic acid) and mobile phase B (acetonitrile with 0.1% formic acid) at a flow rate of 5 μl/min. Positive time-of-flight MS scan was acquired and processed. Peak deconvolution was performed to obtain the distribution profile of DAR0, DAR1, and DAR2 species, and the corresponding peak areas were measured. The relative ratio of each DAR and the average DAR value at each time point were calculated.

Characterization and Quantitation of Catabolites in Tissues

To quantitate the concentrations of payload/catabolites in the mouse plasma and tissues, the tumor samples were homogenized in control mouse plasma, and extracted by an organic solvent (acetonitrile or methanol) to precipitate the proteins. The samples were injected to an AB Sciex Triple Quad 6500 mass spectrometer coupled with a Shimadzu liquid chromatography (LC). Peak separation was achieved by retention times or analyte mass transitions (MRM) and the matrix effects of the tissue samples were minimized by homogenizing the tissues in blank mouse plasma.

DNA-Bound PBD Analysis. DNA isolation and quantitation were performed as described previously (Ma et al., 2016; Zhang et al., 2018). Briefly, mouse tumors were weighed and homogenized in four times the amount of ice-cold phosphate-buffered saline by weight. The plasma samples were diluted with four volumes of ice-cold phosphate-buffered saline. DNA from 75 μl of homogenates was isolated. Aliquots of 200 μl of DNA preparation were digested with 0.001 IU of nuclease P1 at 37°C for 1 hour and then heated at 90°C for 30 minutes to release PBD. Isolated DNA was quantitated by measuring the deoxyadenosine monophosphate generated from nuclease P1 (NP1) digestion with calf thymus DNA as a standard by a liquid chromatography–tandem mass spectrometry (LC-MS/MS) method. The LC-MS/MS analysis showed quantitative recovery of PBD from tissue DNA samples after the digestion. PBD-DNA adduct was calculated on the basis of the conversion of mass of nucleotides as determined by LC-MS/MS to molarity of DNA from the average molecular weight of a DNA base pair (of 650 Da). The results were shown as the adduct numbers per million DNA base pairs. PBD-DNA adducts = PBD concentration/DNA concentration/650×10^6: e.g., at 96 hours, PBD-DNA adducts = $192/(2.73/650 \times 10^9) \times 10^6 = 45.7$ PBD/10^6 bp (Ma et al., 2016).

Measurement of MMAE Concentration in Tumor and Plasma. To determine the concentrations of MMAE in the mouse plasma and tissues, 50 μl of plasma or approximately 50 mg of tumor were mixed with ice-cooled 150 μl of blank mouse plasma. The samples were thoroughly homogenized, two cycles of 30 seconds each, by precooled beads (10 beads, −80°C) and then extracted by ice-cooled 400 μl of acetonitrile/methanol (1:1, v/v) containing 10 nM MMAE-d_8. After a 15-minute centrifugation at 13,500g, 10 μl of supernatant was injected to an AB Sciex Triple Quad 6500 mass spectrometer (Concord, Ontario, Canada) coupled with a Shimadzu liquid chromatography system. Peak separation was achieved using a Phenomenex Kinetex C18 column (Torrance, CA), 1.7 mm, 100 Å, 50 × 2.1 mm with mobile phase A (0.1% formic acid) and B (100% acetonitrile) using a gradient of 0–0.5 minutes 5% B, 0.5–3.5 minutes 5%–90% B, 3.5–4.0 minutes 90% B, 4.0–4.5 minutes 90%–5% B, 4.5–5.0 minutes 5% B at a flow rate of 0.5 ml/min (column temperature of 40°C). The retention time of MMAE and MMAE-d_8 was 2.2 minutes. The MRM transitions in MS were: MMAE, 718.5/686.5, and MMAE-d_8, 726.5/694.5. The compound-dependent MS parameters were 140, 10, 39, 18 for declustering potential (DP), entrance potential (EP), collision energy (CE), and collision cell exit potential (CXP), respectively. The MS instrument-dependent parameters were collision gas (CAD) (–2), curtain gas (CUR) (30), nebulizer gas (GS1) (60), turbo gas (GS2) (60), ion spray voltage (IS) (5500), and ion spray temperature (TEM) (500). The standard curve samples for MMAE quantitation were 0.48–62.5 nM prepared in blank mouse plasma samples and the lower limit of quantification was 0.24 nM.

Quantitation of DM1, DM3, and DM4 and Their Methylated Catabolites in Tumor. To determine the concentrations of these maytansinoids and their methylated catabolites in tumor samples, approximately 50 mg of tumor was mixed with ice-cooled 150 μl of blank mouse plasma. The samples were thoroughly homogenized, two cycles of 30 seconds each, by precooled beads (10 beads, −80°C) and then extracted by ice-cooled 400 μl of acetonitrile/methanol (1:1, v/v) containing 10 nM indomethacin as internal standard (IS). After a 15-minute centrifugation at 13,500g, 10 μl of supernatant was injected to an AB Sciex Triple Quad 6500 mass spectrometer (Concord) coupled with a Shimadzu liquid chromatography system. Peak separation was achieved using a Phenomenex Kinetex C18 column, 1.7 mm, 100 Å, 50 × 2.1 mm with mobile phase A (0.1% formic acid) and B (100% acetonitrile) using a gradient of 0–0.5 minutes 5% B, 0.5–3.5 minutes 5%–90% B, 3.5–4.0 minutes 90% B, 4.0–4.5 minutes 90%–5% B, 4.5–5.0 minutes 5% B

Downloaded from dmd.aspetjournals.org at ASPET Journals on April 18, 2024

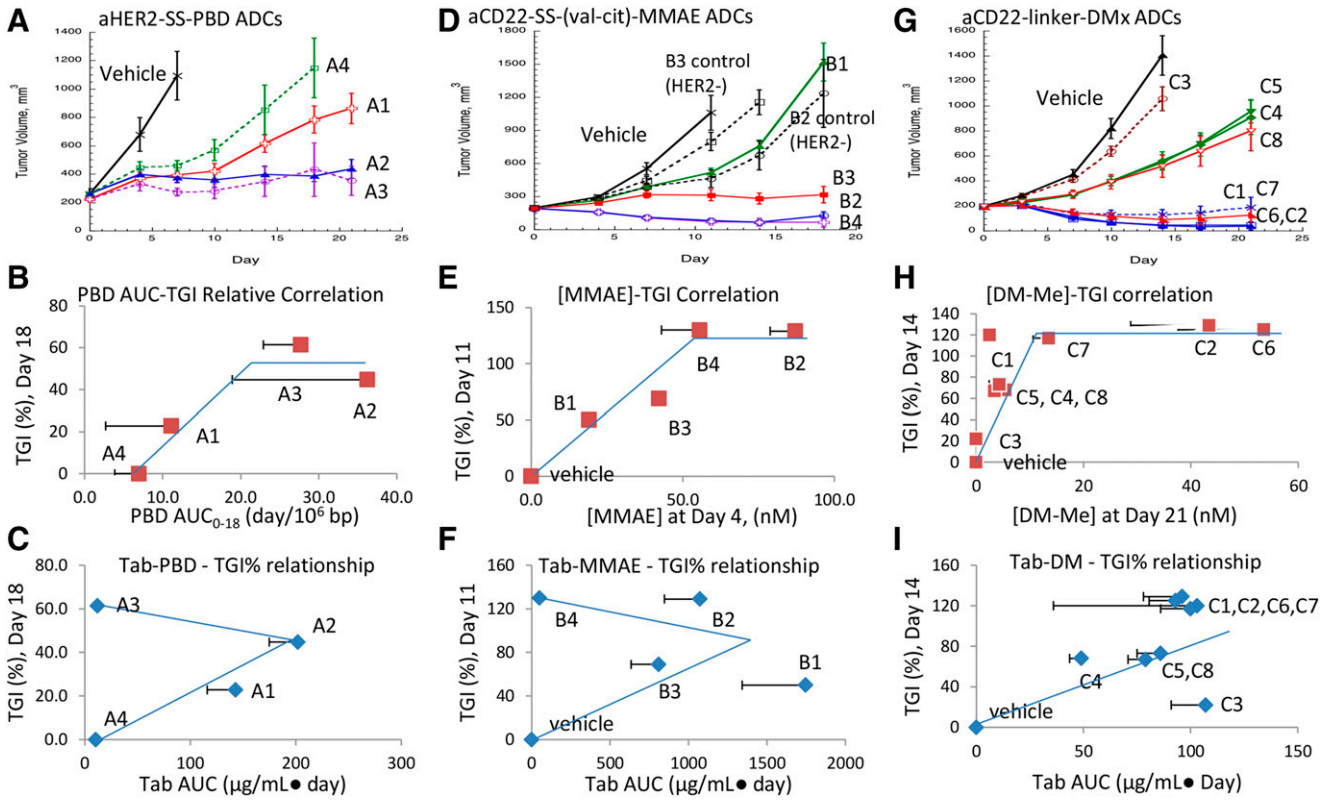

Fig. 2. In vivo efficacy of PBD-, MMAE-, and DMx-ADCs in mice bearing human HER2-expressing Fo5 or human CD22-expressing BJAB.Luc xenografts (n = 8) after intravenous administration of corresponding ADCs A1–A4, B1–B4, C1–C8 (A, D, and G). Correlation X-Y plots of tumor payload/catabolite exposures (PBD, MMAE, or DMx) with TGI_{rel} (B, E, and H). Correlation X-Y plots of plasma total antibody AUC exposures (of PBD, MMAE, or DMx conjugates) with TGI_{rel} (C, F, and I). Part of PBD data has been published (Zhang et al., 2018) and was included here for comparison.

at a flow rate of 0.5 ml/min (column temperature of 35°C). The retention time of DM1, S-methylated DM1, DM3, S-methylated DM3, DM4, S-methylated DM4, and indomethacin were 2.9, 2.9, 3.0, 3.1, 3.1, 3.2, and 3.0 minutes, respectively. The MRM transitions in MS were: DM1, 738.2/547.2; S-methylated DM1, 752.2/188.2; DM3, 766.3/202.1; S-methylated DM3, 780.2/216.0; DM4, 780.1/216.1; S-methylated DM4, 794.2/230.3; indomethacin (IS) 358.0/139.0. The compound-dependent MS parameter was 23–37 for collision energy (CE), 12–24 for collision cell exit potential (CXP), and 10–40 for declustering potential (DP). The MS instrument dependent parameters were collision gas (CAD) (–2), curtain gas (CUR) (30), nebulizer gas (GS1) (60), turbo gas (GS2) (50), ion spray voltage (IS) (5500), and ion spray temperature (TEM) (600). The standard curve samples for DM1/DM3/DM4 quantitation were 1.56–25 nM and the lower limit of quantification was 1.56 nM. The standard curve samples for S-methylated DM1/DM3/DM4 quantitation were 0.24–62.5 nM prepared in blank mouse plasma samples and the lower limit of quantification was 0.24 nM. The matrix effects of the tissue samples were minimized by homogenizing the tissues in blank mouse plasma.

Calculation of ADC and Payload/Catabolite Exposures, Plots with Relative Tumor Growth Inhibition, and Correlation Analysis

The area under the Tab-time curve (AUC) was estimated by a linear trapezoidal method (Perrier and Gibaldi, 1982). For DNA-bound PBD, the intratumoral amount (per 10^6 bp) and concentrations (nanomolar) were determined from tissue collected at days 4, 10, and 18. The area under the PBD amount or concentration-time curve (AUC) was also calculated by a linear trapezoidal method (Perrier and Gibaldi, 1982). These intratumoral PBD exposures were plotted against the relative tumor growth inhibition (TGI_{rel}) (Fig. 2B) (Zhang et al., 2018). The tumor concentrations were determined from tissues collected at day 4 for MMAE, and at day 21 for DM1, DM3, DM4, and their methylated metabolites, and at days 4, 10, and 18 for DNA-bound PBD. These concentrations were plotted against TGI_{rel} (Fig. 2, B, E, and H).

A simple four-parameter correlation analysis was performed for TGI with intratumoral MMAE or DMx-Me exposures from conjugates B1–B4 or C1–C8 in mice bearing human CD22-expressing BJAB.Luc xenografts using Prism 8 (GraphPad Software, San Diego). There were too few data points to allow such analysis for conjugates A1–A4 in mice bearing human HER2-expressing Fo5 xenografts. Spearman's correlation analysis was also performed with SPSS software (version 22.0; SPSS Inc., Armonk, NY) to examine the relationships between intratumoral payload exposure (payload AUC) and corresponding TGI%, between total antibody exposures (Tab AUC) and TGI, and between intratumoral payload exposure (payload AUC) and total antibody exposures (Tab AUC) for all three sets of experimental data. Statistical significance was set at $P < 0.05$.

Results

Table 1 lists the ADC structures, animal model parameters, systemic ADC exposures, and efficacy for ADCs A1–A4 (anti-HER2-PBD conjugates), B1–B4 (anti-CD22-MMAE conjugates), and C1–C8 (anti-CD22-DMx conjugates). In these three sets of experiments, the antibody was the same for a given set and the payload was either the same (for MMAE and PBD) for conjugates A1–A4 and B1–B4 or had the same pharmacological activity (for DM1, DM3, and DM4) for conjugates C1–C8. Figure 1 lists the chemical structures of all ADC molecules and payloads/catabolites used in this study. The total antibody (Tab) concentrations plotted against three time points for animals dosed with anti-HER2-PBD, anti-CD22-MMAE, and anti-CD22-DMx conjugates are shown in Fig. 3, A, D, and G. The average Tab-AUC values for each treatment group are plotted in Fig. 3, B, E, and H, and the trend lines were drawn in the Tab AUC versus tumor growth inhibition X-Y plots. The time profiles of total antibody concentration and normalized average drug-to-antibody ratios (representing the stabilities of ADCs) are shown in Fig. 3, C, F, and I.

Downloaded from dmd.aspetjournals.org at ASPET Journals on April 18, 2024

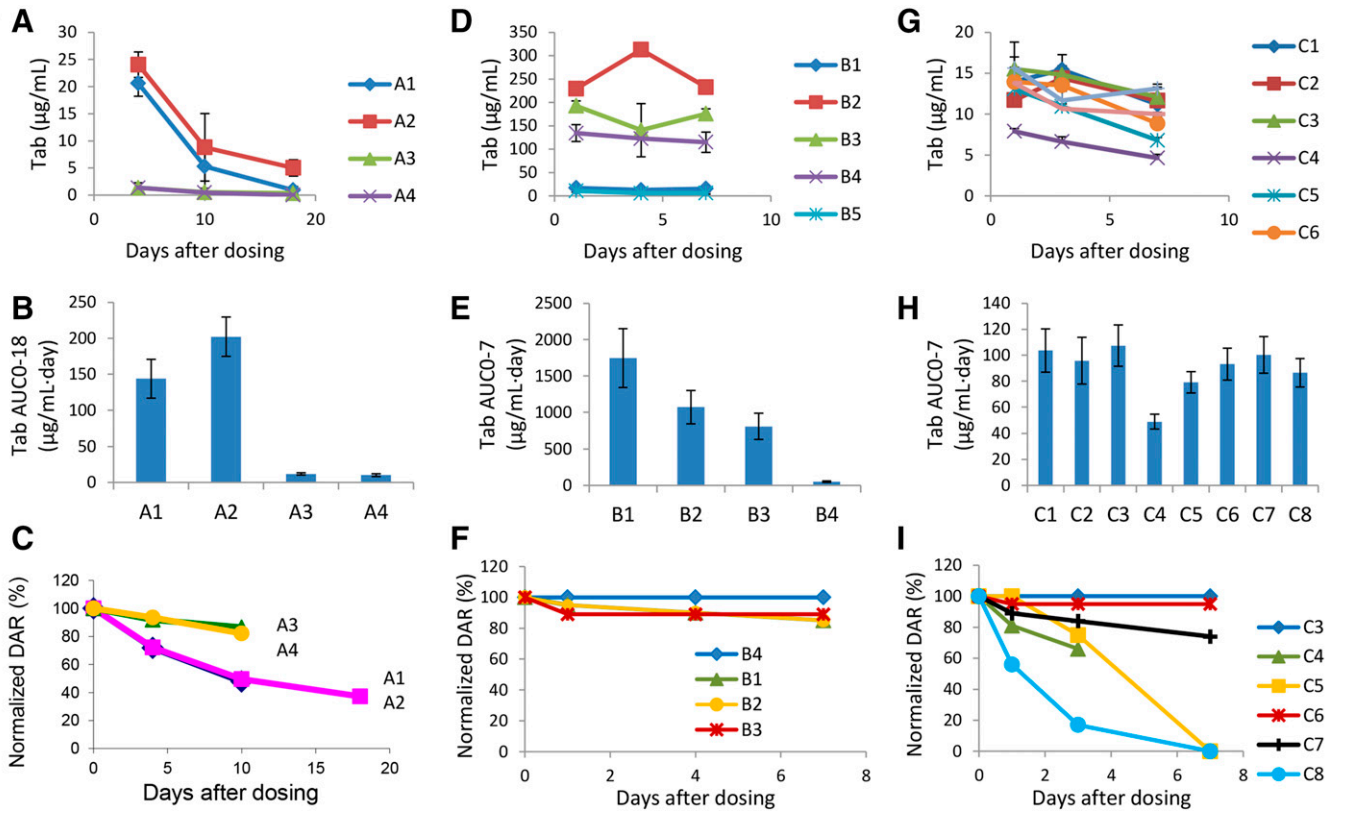

Fig. 3. Total antibody concentration and time profiles in plasma of xenograft mice following intravenous administration of corresponding ADCs A1–A4, B1–B4, and C1–C8 (A, D, and G). Total antibody AUC values calculated from concentration data in Supplemental Table S2 of selected time points of 0–18 days for PBD-ADC and 0–7 days for MMAE- and DMx-ADCs (B, E, and H). Normalized antibody-to-drug ratios and time profiles in plasma (C, F, and I). Part of PBD data has been published (Zhang et al., 2018) and was included here for comparison.

All dosing regimens were tolerated well in mice without any body weight loss or adverse clinical symptoms observed (Supplemental Fig. S2). Multiple parameters were examined for trend correlation with the observed efficacy in xenograft models. Importantly, Fig. 2 and Supplemental Fig. S1 show that relative tumor growth inhibition (TGI_{rel}, efficacy) (Yu et al., 2015) increased with intratumoral payload concentrations or amounts but did not correlate with ADC systemic exposures (total antibody AUC) following intravenous administration of various ADCs.

The trend correlation was observed for TGI with intratumoral PBD, MMAE, and DMx exposures, and the correlations between TGI and intratumoral MMAE or DMx-Me exposures had some significance (Supplemental Figs. S3 and S4) from a four-point correlation analysis. Spearman's correlation analysis showed correlation (correlation coefficient of 0.79–0.90) with statistical significance (Table 2) between intratumoral MMAE and DMx exposures and TGI in the CD22-expressing BJAB.Luc xenograft models. For HER2-PBD conjugates in the HER2-expressing Fo5 xenograft models, there is a correlation (correlation coefficient of 0.8–1.0) but that is only statistically significant when S.D. was corrected for conjugate A2 (Table 2). Spearman's correlation analysis showed no correlation (Table 2) between TGI and total antibody exposures for all three sets of experiments (Table 2). There is no correlation between intratumoral payload exposures and total antibody exposures for all three sets of experiments (Table 2).

Anti-HER2-PBD ADCs. Figure 2B shows that there is a trend correlation between antitumoral activity and intratumoral PBD exposures in HER2-expressing MMTV-Fo5 allograft models following single doses of ADCs A1–A4 (Table 1). These four ADCs incorporate two types of disulfide linkers (non-methyl disulfide and methyl disulfide) and two attachment sites (light chain K149C and heavy chain A140C) and two doses (4 and 0.4 mg/kg) were employed in the described experiments (Fig. 1; Table 1) (Ma et al., 2016; Zhang et al., 2018). In this study, the subcellular amount of PBD bound to DNA was determined and correlated with TGI_{rel} values of ADC conjugates A1, A2, and A3 relative to the days 0–18 tumor growth curve of ADC A4. For this analysis, the vehicle control animals in the Fo5 efficacy study were terminated at day 7 due to rapid tumor growth and could thus not be used for standard TGI calculations (Pillow et al., 2014; Yu et al., 2015). Relative comparisons of 0–18-day tumor growth inhibition were made among the different conjugates with that of the least-active entity (A4). As shown in Fig. 2B, the increased intratumoral PBD exposures corresponded to the higher levels of antitumoral activity with intratumoral PBD $AUC_{0–18}$ values (AUC during 0–18 days) in excess of 20 days/10^6 bp affording a maximum level of efficacy ("Plateau"). Similar trend correlations were obtained when the AUC (0–18 days) of PBD covalently bound to DNA (Fig. 2B), AUC of intratumoral PBD concentrations, or PBD amounts in days 4, 10, or 18 tumors were used (Zhang et al., 2018). In addition, when tumor sizes (Y-axis) from all groups at all-time points were plotted against the PBD amount (X-axis) in the corresponding groups, the PBD amount needed to be approximately 1/10^6 PBD/bp to achieve tumor stasis as a threshold. Importantly, payload amounts in tumor increased for all four conjugates from day 4 to day 10, but for only ADCs A2 and A3, the amounts of the PBD payload reached an initial threshold to support the tumor growth inhibition and the value was not significantly diminished over 3 weeks following single doses. In comparison, an initial threshold of PBD amount was not reached for tumor stasis for ADCs A1 and A4 to support the efficacy (Zhang et al., 2018).

Downloaded from dmd.aspetjournals.org at ASPET Journals on April 18, 2024

TABLE 2

The Spearman correlation analysis of intratumoral payload exposure (payload AUC) vs. TGI%, total antibody exposure (Tab AUC) vs. TGI%, and intratumoral payload exposure (payload AUC) vs. total antibody exposure (Tab AUC)

	TGI vs. Intratumoral Payload AUC		TGI vs. Tab AUC		Intratumoral Payload AUC vs. Tab AUC	
	Correlation Coefficient	Sig (Two-Tailed)	Correlation Coefficient	Sig (Two-Tailed)	Correlation Coefficient	Sig (Two-Tailed)
HER2-PBD ADCs A1-A4 (in Fig. 2, B and C)	0.800	0.200	0.800	0.300	0.443	0.553
HER2-PBD ADCs A1-A4 (in Fig. 2, B and C)[a]	1.000[a]	0.000*				
CD22-MMAE ADCs B1-B4 (in Fig. 2, E and F)	0.795	0.010*	0.383	0.308	0	1.0
CD22-DMx ADCs C1-C8 (in Fig. 2, H and I)	0.900	0.037*	0.100	0.873	0.300	0.624

Sig, significance.
*$P < 0.05$.
[a]When data of conjugate A2 was corrected by S.D.

Systemic exposures (AUC of total antibody) did not correlate with the tumor growth inhibition (Fig. 2C). The normalized DAR values of ADC A1, A2, A3, or A4 were not greatly reduced, which suggested that there were sufficient conjugated antibodies in circulation of mouse for up to 17 days after dose (Fig. 3C). Attachment sites and linker types did not consistently affect the ADC stability (Figs. 2, A–C and 3, A–C), which in turn might have afforded the different intratumoral payload levels observed, especially at later time points for these ADCs (Zhang et al., 2018). These results indicated that the antitumoral efficacy showed trend correlation with the intratumoral PBD exposures with a "plateau" effect.

Anti-CD22-MMAE ADCs. We next wanted to determine whether the trends noted with the PBD-containing ADCs described above were also observed with conjugates bearing other classes of cytotoxic payloads. Accordingly, we assessed the concentrations of MMAE (a well known tubulin-binding antimitotic agent) in CD22-expressing BJAB tumors following single intravenous administration of several CD22-targeting ADCs. In these experiments, we measured MMAE concentrations in homogenized tumor tissues, as we were not able to accurately quantitate such levels in specific microtubule-related compartments. As was observed for the PBD-containing ADCs described above, a correlation was achieved between intratumoral MMAE concentrations and the corresponding efficacies in the BJAB model (Fig. 2, D and E; TGI% relative to vehicle control during days 0–11).

Importantly, as was the case with the PBD-containing ADCs, measurement of intratumoral payload concentrations afforded rationalizations of the observed efficacies. The methyl-disulfide (Me-SS-)-MMAE ADC B1 only showed approximately 50% tumor growth inhibition after a 20-mg/kg dose (Fig. 2, D and E). Linker modification with dimethyl disulfide (DiMe-SS-) (ADC B3) improved the payload delivery to tumor (to 42.1 nM) with corresponding improved TGI to 69%. The Val-Cit peptide linker MMAE-ADC B4 delivered 55.6 nM MMAE to the tumors even at 1-mg/kg dose and to give a corresponding 30% tumor regression. Additional payload delivery (87.1 nM) by addition of PAB group to the disulfide linker (ADC B2) at 20-mg/kg dose did not further improve tumor regression compared with ADC B4. The intratumoral MMAE concentration appeared to reach approximately 50 nM to "plateau" antitumoral activity. The peptide linker ADC B4 had lowest systemic total antibody exposure but delivered a high level of payload to support the corresponding efficacy (Fig. 2, D–F). Intratumoral MMAE concentrations increased 6-fold (from 3.3 to 19.1 nM) with the 20-fold increased dose of Me-disulfide-linker MMAE ADC B1 (from 1 to 20-mg/kg dose, comparison of group B1 with group B1_1 in Table 1) (Supplemental Table S1A). In comparison, the dose of 20 mg/kg of the Me-disulfide-MMAE ADC (ADC B1) resulted in an almost proportional 20-fold higher circulating total antibody than the 1-mg/kg dose of the same ADC B1 or the 1-mg/kg dose of the Val-Cit-PAB-MMAE ADC B4 (Figs. 2G and 3, D and E). Different concentrations of MMAE in tumors from these ADCs suggested that the linker made a significant difference in the payload delivery to tumors.

Lack of correlation was observed between exposures of total antibody and tumor growth inhibition (Fig. 2F), which was not the result of instability of any ADC conjugate. All ADC conjugates were stable in mouse plasma for up to 7 days of testing (Fig. 3F).

Anti-CD22-DMx-ADCs. We also explored whether the above trends and relationships could be observed with an alternate tubulin-binding ADC payload class. As part of these new experiments, we also wished to assess the feasibility of intratumoral catabolite quantitation at a relatively late time-point when tumors associated with highly active conjugates were relatively small in size at the study termination. Accordingly, we assessed the day-21 intratumoral concentrations of bioactive S-methylated and thiol-containing catabolites from ADC linker-payloads derived from the cytotoxic maytansinoids DM1, DM3, and DM4 (Fig. 1). As was the case with the MMAE-containing conjugates discussed above, the new assessments were performed following single intravenous administration of several CD22-targeting ADCs in CD22-expressing BJAB tumors (total tumor tissue homogenates). The S-methylated catabolites of maytansinoids DM1, DM3, and DM4 showed cell-killing potency at similar pM concentrations that were >10-fold more potent than DM1, DM3, and DM4 (thiol forms) (Erickson and Lambert, 2012; Widdison et al., 2015). These thiol-containing compounds showed much more potent cell-killing activity (>10-fold) than other forms of maytansinoid catabolites. Therefore, the thiol and methylated forms of DM1, DM3, or DM4 should be responsible for the efficacy and toxicity of their corresponding ADCs, and were, therefore, quantified and plotted against the efficacy of tumor growth inhibition. A conjugate bearing a non-cleavable (MPEO, C3) linker was also included for comparison.

Figure 2, G and H showed that the days 0–21 tumor growth inhibition efficacy (compared with vehicle controls) in the CD22-expressing BJAB model improved with day-21 tumor concentrations of methylated DM1, DM3, and DM4, but the efficacy reached a "plateau" above approximately 10–15 nM of catabolite concentrations in the tumor. As was noted for the PBD- and MMAE-containing entities discussed above, an intratumoral threshold concentration was potentially defined by the collected data beyond which only minimal efficacy improvements were observed (approximately 13 nM of the S-methylated catabolites from comparison of C2 and C6 with C1 and C7 in Fig. 2H; Supplemental

Downloaded from dmd.aspetjournals.org at ASPET Journals on April 18, 2024

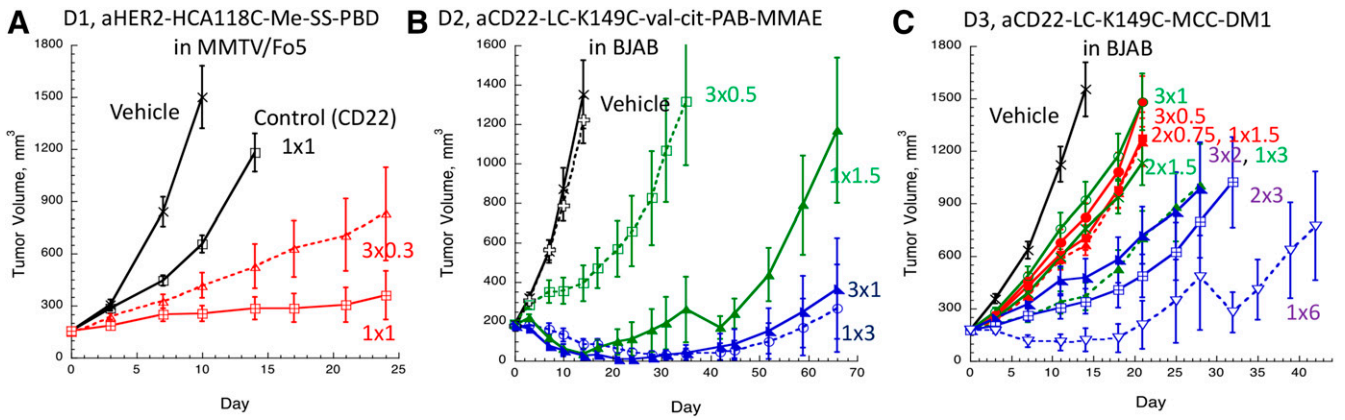

Fig. 4. Dose-fractionation efficacy studies of PBD-, MMAE-, and DM1-containing ADCs D1, D2, and D3 in xenograft models. Xenograft mice (n = 8 each treatment group) were dosed with a single intravenous dose or one-third or one-half of the dose every week three times or twice (A–C). Tumors in mice were measured one to two times a week throughout the studies. The tumor volumes were plotted as a mean tumor volume S.E.M. of each group over time.

Fig. S1). Direct conjugation of DM4 to FcS400C (ADC C7) delivered more payload of S-methylated catabolites to tumors than those of DM4 with a longer and hetero-bifunctional linker in ADCs C4 and C5, which in turn delivered more than the noncleavable linker (ADC C3) (Fig. 2H; Supplemental Table S1B). These catabolite concentrations showed a correlation with the corresponding efficacy (Fig. 2H). Direct conjugation of DM3 and DM4 (ADCs C2, and C6) at light chain attachment K149C delivered approximately twice more payload than the Fc attachment S400C (ADC C7) but without further improving efficacy (Fig. 2, G and H). A similar correlation was observed when a combined concentration of a thiol and its methylated forms of DM1, DM3, and DM4 was used (Supplemental Fig. S1).

As was noted with PBD and MMAE ADCs, it is difficult to correlate the ADC stability measured by DAR values (Fig. 3I) and total antibody (Tab) concentrations to the corresponding efficacy (Fig. 2I). ADC C7 showed DAR loss over time but had one of the best efficacies. In contrast, ADC C3 showed stability without DAR loss but had marginal tumor growth inhibition activity (Fig. 2, G and H; Table 1). The hetero-bifunctional linkers in ADCs C4 and C5 showed lower Tab exposures and DAR losses (Fig. 3, G–I). Direct conjugation of DM4 to light chain at K149C (ADC C6) showed stable levels of total antibody over 7-day measurements with no DAR loss at day 10 (Table 1). However, direct conjugation of DM3 to Fc region at S400C (ADC C8) showed complete loss of the payload (DAR = 0 at day 10) although the levels of total antibody over 7-day measurements remain high (Fig. 3, G–I; Table 1).

Collectively, these results demonstrate that intratumoral quantitation of bioactive catabolites or payloads associated with a third class of well known ADC payloads can clearly rationalize in vivo efficacy outcomes and provide clarity regarding ADC in vivo efficacy relative to assessments of in vivo total antibody and/or stability, dose, or linker.

Dose-Fractionation Studies. The above correlation results of tumor growth inhibition with intratumoral payload/catabolite exposures suggest that the intratumoral payload/catabolite concentration drives the ADC efficacy. To test whether there is a threshold payload concentration needed for efficacy, we performed dose fractionation studies to compare with the efficacy results from the single doses and fractionated doses. In Fig. 4A, a single 1-mg/kg dose of an anti-HER2-Me-SS-PBD ADC (conjugate D1) showed tumor stasis in the MMTV-Her2/Fo5 model for over 3 weeks, but when this dose was administered each week three times at 0.3 mg/kg, only partial tumor growth inhibition was achieved. A much lower level of efficacy was observed with the non-target ADC (anti-CD22-control) in these experiments. Although the total dose and total systemic antibody exposures from 1 mg/kg and 3 × 0.3 mg/kg were similar, the single dose showed a much better efficacy. A smaller initial dose could not supply a sufficient concentration of payload to cause tumor growth inhibition and additional doses did not further improve the partial efficacy (did not break the trend of tumor growth). Consistent with our intratumoral PBD analysis results in the last study, once a threshold intratumoral PBD concentration is reached to achieve an antitumoral activity (tumor stasis) from an initial 1-mg/kg dose, no additional doses were needed to sustain the tumor stasis or tumor reduction for up to 3–6 weeks (Zhang et al., 2018).

To test if a microtubule inhibitor ADC also shows the requirement of a threshold concentration, anti-CD22-Val-Cit-PAB MMAE ADC (conjugate D2) was dosed with a four-dose regimen. Figure 4B shows that the MMAE-ADC had a better efficacy after a single 1.5-mg/kg dose than the fractionated dose that was administered every week three times (3 × 0.5 mg/kg). In the same experiment, a single 3 mg/kg showed a similar efficacy with a fractionated 3 × 1 mg/kg dosing regimen. The latter results clearly demonstrated that excessive delivery of MMAE payload to tumor did not further improve the efficacy (Fig. 4B), which supported the earlier result of "plateau" efficacy observations (Fig. 2E).

Figure 4C shows that a single 6-mg/kg dose of an anti-CD22-MCC-DM1 ADC (conjugate D3) showed a better efficacy than the dose administered twice (2 × 3 mg/kg), which was better than the dose administered three times (3 × 2 mg/kg). Likewise, a single 3-mg/kg dose of conjugate D3 showed a better efficacy than the dose administered twice (2 × 1.5 mg/kg) which was better than the dose administered three times (3 × 1 mg/kg). Further fractionation did not differentiate the dose regimen as a single 1.5-mg/kg dose of conjugate D3 showed a similar partial tumor growth inhibition efficacy as the dose administered twice (2 × 0.75 mg/kg) or the dose administered three times (3 × 0.5 mg/kg). Collectively, the results from all three cases that use different payloads in different ADCs in different tumor models support that a minimal dose is required for sustained efficacy and fractionated doses did not demonstrate the same level of efficacy to the single doses. The minimal dose presumably resulted in a threshold payload concentration to support the efficacy.

Discussion

ADCs are structurally complex molecules that have different mechanisms for uptake, distribution, and metabolism from those of traditional small-molecule drugs. In addition, many disease target–related and patient (xenograft models)-related variables such as tumor types, antigen types and expression could impact ADC efficacy and

Downloaded from dmd.aspetjournals.org at ASPET Journals on April 18, 2024

toxicity. To be efficacious, an ADC from circulation needs to bind to tumor cell surface antigens and become internalized and degraded in lysosomes. The payload is released and engaged with the target. Although an ADC helps deliver the payload to tissues, the payload is ultimately responsible for efficacy and toxicity. A threshold concentration of payload over time in target tissues would be required to trigger and support efficacy (Zhang et al., 2019). In this study, we intended to use ADCs with multiple linkers, attachment sites, and doses to modulate the intratumoral payload delivery in xenograft models. At the same time, ADC exposure data from the dosed animals with various ADCs were collected and relationships between various ADC exposures (Tab AUC) with associated variables (e.g., DAR changes) and TGI were analyzed. Consequently, the study designs appeared to be relatively complicated with ADCs of three payload types in multiple xenograft models. These experimental designs allowed us to test many relevant variables of an ADC in relatively simplified set of experiments. The result was that we were able to find preliminary trend correlation or lack of correlation between these variables.

The plasma stability of ADCs, linkers, and conjugation sites did not markedly affect ADC exposures, but the doses were proportionally related to ADC exposures in circulation. Among all ADCs used, only a few conjugates (disulfide conjugates A1, A2, C4, C5, and C8) showed instability with DAR loss but which only decreased total ADC exposures to a limited extent, and approximately >50% of the high Tab AUC values still remained (comparing conjugates A1 and A2 or conjugates C4, C5, and C8). In comparison, the ADC exposures (Tab AUC) increased directly with the doses in a given set of experiments. For example, conjugate A1 showed approximately 10-fold Tab AUC of that for conjugate A3 as does the dose despite that A1 showed DAR loss. The dose 20 mg/kg of the Me-disulfide-MMAE ADC (ADC B1) resulted in an almost proportional 20-fold higher circulating total antibody (Tab) than the 1-mg/kg dose of the same conjugate. Disulfide-linked conjugate B1 and Val-Cit-PAB-MMAE conjugate B4 had similar Tab AUC at a 1-mg/kg dose. The DAR loss appeared to be consistent with the less stable linkers in A1 and A2 compared with the substituted and more stable linkers in A3 and A4. The instability of C8 with DAR loss appeared to be related to the unstable Fc attachment site.

The linkers made significant differences in the payload delivery to tumors. The more stable disulfide linker in A3 delivered three times the PBD payload to tumors than that from A1 with a less stable linker and 10% of the dose (0.4 vs. 4 mg/mg). Conjugate A3 delivered approximately a similar level of PBD payload to tumors as A2, which had a less stable linker but a more stable attachment site with 10% of the dose (0.4 vs. 4 mg/kg). The Val-Cit peptide linker (in B4) at 1 mg/kg delivered a similar and efficacious level of MMAE to tumors as did the PAB disulfide linker (ADC B2) at 20-mg/kg dose. In comparison, for the same ADC (with the same linker), intratumoral MMAE concentrations increased less proportionally with the dose as the intratumoral MMAE concentration increased 6-fold compared with the 20-fold increases of dose for Me-disulfide-linker MMAE ADC B1 (group B1_1 vs. group B1 in Supplemental Table S1A). A higher dose of the same ADC used in the fractionation presumably would also have delivered a higher level of payload to tumors. Therefore, the linker and dose together appear to be key parameters determining the payload concentrations in tissues.

To relate the efficacy with intratumoral payload concentrations, intratumoral PBD AUC values or amounts at days 4, 10, and 18 correlated with days 0–21 tumor growth inhibition in a HER2-tumor model. Intratumoral MMAE concentrations at day 4 correlated with days 0–11 tumor growth inhibition in a CD22-tumor model. Finally, intratumoral DMx concentrations at day 21 correlated with days 0–21 tumor growth inhibition in a CD22-tumor model. In contrast, total antibody exposures do not correlate with the efficacy of tumor growth inhibition in all three models tested. Use of total payload concentrations instead of free payload fraction in tumors for correlation is logical since PBD covalently bound to target DNA, and MMAE and DMx tightly bound to the target microtubules. In these trend correlation relationships as expressed by X-Y plots (Fig. 2, B, E, and H), there appeared to be 1) an improving efficacy with increasing payload amounts or concentrations followed by a plateau; 2) a region of oversupply of payload in which increased payload concentration stopped improving tumor growth regression ("plateau" effect); and 3) a minimal threshold payload concentration that is required to support tumor stasis. These results also suggest that the three classes of ADCs in this study all have a payload tissue maximum concentration C_{max}-driven exposure-efficacy correlation. The threshold payload concentration in tumors for efficacy was approximately 1 PBD/10^6 bp for PBD-ADC and 50 nM for MMAE-ADCs, and 13 nM for DMx-ADCs. Because these payloads represented different mechanisms of cell killing, were used in different animal models, and had other different intrinsic properties, these threshold efficacious concentrations are different for the three classes of ADCs investigated in this study. These preliminary trend correlations of tissue payload concentration with tumor growth inhibition with different ADCs in different animal models may stimulate a large scale of experiments with more comprehensive statistical analyses.

There did not appear to be any correlation between efficacy and systemic exposures of ADCs along with linker, site of payload attachment, and plasma stability. Lack of correlation between the systemic exposure and efficacy is not surprising since the circulating ADC is required to get to tumors and to release the payload properly for activities. ADCs with unstable sites of attachment leading to fast clearance and low efficacy might actually never deliver a threshold concentration of payload to tumors to achieve efficacy (Shen et al., 2012; Kamath and Iyer, 2015; Lin et al., 2015). As implied from results of several sets of experiments in this study, there was lack of correlation between payload delivery and total ADC exposure. A physiologically based pharmacokinetic modeling approach to link plasma ADC exposure with tissue payload concentration to tumor growth inhibition would be useful to inform clinical dose levels and schedules given the limitation in collecting clinical tissues.

Payload delivery to the site of action by an ADC is limited by antigen-mediated uptake and pinocytosis, as well as pharmacokinetic and dispositional characteristics of the antibody. Consequently, drug delivery by an ADC is slow compared with the delivery of small-molecule drugs that depend on fast/direct uptake, or concentration difference–dependent intrinsic absorption after oral administration (Wang et al., 2008; Sliwkowski and Mellman, 2013; Polakis, 2016). ADCs attenuate the maximum concentration C_{max} of the payload in circulation and tissues, and slow down and prolong the payload supply. This propensity is favorable to decreasing the toxicity of ADCs. Therefore, the exposure-response (efficacy or toxicity) relation of an ADC could be different from, sometimes contrary to, a small-molecule drug in that a higher systemic exposure may not lead to a higher level of tissue delivery of a drug for efficacy and toxicity.

An important observation from these data was that the intratumoral payload concentrations reached a plateau concentration beyond which additional efficacy was not achieved. Recognition of payload concentrations for efficacy-to-"plateau" is important, as extra payload delivery to tumors does not improve efficacy but may generate a higher catabolite concentration in normal tissues that may cause toxicity. In addition, a minimal and efficacious dose and threshold drug concentration in tumors can be defined through dose fractionation studies in preclinical animal models. The translation of these results to the clinic with xenograft animal models is not known.

Downloaded from dmd.aspetjournals.org at ASPET Journals on April 18, 2024

However, these experiments and observations support the clinical principles described by the recent European Medicines Agency. These principles in "Guideline on strategies to identify and mitigate risks for first-in-human and early clinical trials with investigational medicinal products" (www.ema.europa.eu/EMEA/CHMP/SWP/28367/07) include: 1) Target saturation should be taken into account when appropriate, and then the maximum exposure should consider when complete inhibition or activation of the target is achieved and no further therapeutic effect is to be expected by increasing the dose; 2) a clinic trial using a maximum tolerable dose approach is considered inappropriate for healthy volunteers; 3) a starting dose that is substantially lower than the human expected pharmacological dose may not be appropriate; and 4) appropriate nonclinical studies need to be performed to define the minimum pharmacologically active dose. Prolonged target engagement of PBD through covalent binding to target DNA and MMAE or DM1 through tight binding to microtubule proteins may support dose and/or frequency alterations to minimize toxicity. The current ADC dosing schedule of every 3 weeks may lead to the extra payload delivery that may not improve the antitumoral efficacy but would generate more payload in normal tissues, leading to toxicity. The studies reported here tried to take advantage of the limited tumor samples collected at termination or at selected time points of satellite groups in the same efficacy studies. Our results suggest that the assessment of the intratumoral payload amounts or concentrations to support a maximal efficacy should be achievable in xenograft models first, which could be useful for design of an optimal ADC and dosing regimen in the clinic.

In summary, this study demonstrates that: 1) the plasma stability of ADCs, the linkers, and conjugation sites does not markedly affect ADC exposures, but the dose is directly related to ADC exposures in circulation; 2) the linker and dose together made significant differences in the payload delivery to tumors; and 3) intratumoral payload concentrations correlate with ADC efficacy and that the efficacy is saturable (i.e., plateaus) after a threshold intratumoral payload concentration is reached. These concepts provided insights for ADC efficacy in two important aspects. First, ADC optimization should not rely on traditional pharmacokinetic studies of systemic exposures of ADC species since a correlation between ADC plasma concentrations and efficacy is not known. Second, a threshold concentration of intratumoral payload is required to support sustained efficacy. Importantly, an ADC can deliver payloads beyond this threshold that are excessive and do not enhance efficacy ("plateau" effect).

Acknowledgments

We thank Geoffrey Del Rosario, Jintang He, Corinna Lei, Luna Liu, and Hans Erickson for their technical contributions and Dr. Eugene Chen from Genentech, who helped with 4-parameter correlation analysis.

Authorship Contributions

Participated in research design: Zhang, Dragovich, Yu, Khojasteh, Hop.

Conducted experiments: Ma, Yu.

Contributed new reagents or analytic tools: Pillow, Sadowsky.

Performed data analysis: Zhang, Yu, Dragovich, Khojasteh, Su, Wang, Polson, Hop.

Wrote or contributed to the writing of the manuscript: Zhang, Dragovich, Yu, Khojasteh, Hop.

References

Antonow D and Thurston DE (2011) Synthesis of DNA-interactive pyrrolo[2,1-c][1,4]benzodiazepines (PBDs). *Chem Rev* **111**:2815–2864.

Beck A, Goetsch L, Dumontet C, and Corvaïa N (2017) Strategies and challenges for the next generation of antibody-drug conjugates. *Nat Rev Drug Discov* **16** (5):315–337, doi: 10.1038/nrd.2016.268 28303026.

Bhakta S, Raab H, and Junutula JR (2013) Engineering THIOMABs for site-specific conjugation of thiol-reactive linkers. *Methods Mol Biol* **1045**:189–203.

Doronina SO, Toki BE, Torgov MY, Mendelsohn BA, Cerveny CG, Chace DF, DeBlanc RL, Gearing RP, Bovee TD, Siegall CB, et al. (2003) Development of potent monoclonal antibody auristatin conjugates for cancer therapy. *Nat Biotechnol* **21**:778–784.

Erickson HK and Lambert JM (2012) ADME of antibody-maytansinoid conjugates. *AAPS J* **14**: 799–805.

Jeffrey SC, Burke PJ, Lyon RP, Meyer DW, Sussman D, Anderson M, Hunter JH, Leiske CI, Miyamoto JB, Nicholas ND, et al. (2013) A potent anti-CD70 antibody-drug conjugate combining a dimeric pyrrolobenzodiazepine drug with site-specific conjugation technology. *Bioconjug Chem* **24**:1256–1263.

Junutula JR and Gerber HP (2016) Next-generation antibody-drug conjugates (ADCs) for cancer therapy. *ACS Med Chem Lett* **7**:972–973.

Kamath AV and Iyer S (2015) Preclinical pharmacokinetic considerations for the development of antibody drug conjugates. *Pharm Res* **32**:3470–3479.

Kozak KR, Tsai SP, Fourie-O'Donohue A, dela Cruz Chuh J, Roth L, Cook R, Chan E, Chan P, Darwish M, Ohri R, et al. (2013) Total antibody quantification for MMAE-conjugated antibody-drug conjugates: impact of assay format and reagents. *Bioconjug Chem* **24**:772–779.

Lewis Phillips GD, Li G, Dugger DL, Crocker LM, Parsons KL, Mai E, Blättler WA, Lambert JM, Chari RV, Lutz RJ, et al. (2008) Targeting HER2-positive breast cancer with trastuzumab-DM1, an antibody-cytotoxic drug conjugate. *Cancer Res* **68**:9280–9290.

Lin K, Rubinfeld B, Zhang C, Firestein R, Harstad E, Roth L, Tsai SP, Schutten M, Xu K, Hristopoulos M, et al. (2015) Preclinical development of an anti-NaPi2b (SLC34A2) antibody-drug conjugate as a therapeutic for non-small cell lung and ovarian cancers. *Clin Cancer Res* **21**:5139–5150.

LoRusso PM, Weiss D, Guardino E, Girish S, and Sliwkowski MX (2011) Trastuzumab emtansine: a unique antibody-drug conjugate in development for human epidermal growth factor receptor 2-positive cancer. *Clin Cancer Res* **17**:6437–6447.

Ma Y, Khojasteh SC, Hop CE, Erickson HK, Polson A, Pillow TH, Yu SF, Wang H, Dragovich PS, and Zhang D (2016) Antibody drug conjugates differentiate uptake and DNA alkylation of pyrrolobenzodiazepines in tumors from organs of xenograft mice. *Drug Metab Dispos* **44**:1958–1962.

Perrier D and Gibaldi M (1982) General derivation of the equation for time to reach a certain fraction of steady state. *J Pharm Sci* **71**:474–475.

Pillow TH, Tien J, Parsons-Reponte KL, Bhakta S, Li H, Staben LR, Li G, Chuh J, Fourie-O'Donohue A, Darwish M, et al. (2014) Site-specific trastuzumab maytansinoid antibody-drug conjugates with improved therapeutic activity through linker and antibody engineering. *J Med Chem* **57**:7890–7899.

Polakis P (2016) Antibody drug conjugates for cancer therapy. *Pharmacol Rev* **68**:3–19.

Polson AG, Williams M, Gray AM, Fuji RN, Poon KA, McBride J, Raab H, Januario T, Go M, Lau J, et al. (2010) Anti-CD22-MCC-DM1: an antibody-drug conjugate with a stable linker for the treatment of non-Hodgkin's lymphoma. *Leukemia* **24**:1566–1573.

Ricart AD (2011) Antibody-drug conjugates of calicheamicin derivative: gemtuzumab ozogamicin and inotuzumab ozogamicin. *Clin Cancer Res* **17** (20):6417–6427, doi: 10.1158/1078-0432.CCR-11-0486 22003069.

Sadowsky JD, Pillow TH, Chen J, Fan F, He C, Wang Y, Yan G, Yao H, Xu Z, Martin S, et al. (2017) Development of Efficient Chemistry to Generate Site-Specific Disulfide-Linked Protein- and Peptide-Payload Conjugates: Application to THIOMAB Antibody-Drug Conjugates. *Bioconjug Chem* **28** (8):2086–2098, doi: 10.1021/acs.bioconjchem.7b00258 28636382.

Shen BQ, Xu K, Liu L, Raab H, Bhakta S, Kenrick M, Parsons-Reponte KL, Tien J, Yu SF, Mai E, et al. (2012) Conjugation site modulates the in vivo stability and therapeutic activity of antibody-drug conjugates. *Nat Biotechnol* **30**:184–189.

Shor B, Gerber H-P, and Sapra P (2015) Preclinical and clinical development of inotuzumab-ozogamicin in hematological malignancies. *Mol Immunol* **67** (2 Pt A):107–116, doi: 10.1016/j.molimm.2014.09.014 25304309.

Sliwkowski MX and Mellman I (2013) Antibody therapeutics in cancer. *Science* **341**:1192–1198.

Su D, Kozak KR, Sadowsky J, Yu S-F, Fourie-O'Donohue A, Nelson C, Vandlen R, Ohri R, Liu L, Ng C, et al. (2018) Modulating Antibody-Drug Conjugate Payload Metabolism by Conjugation Site and Linker Modification. *Bioconjug Chem* **29** (4):1155–1167, doi: 10.1021/acs.bioconjchem.7b00785 29481745.

Wang W, Wang EQ, and Balthasar JP (2008) Monoclonal antibody pharmacokinetics and pharmacodynamics. *Clin Pharmacol Ther* **84**:548–558.

Wei C, , Su D, , Wang J, , Jian W, and , Zhang D (2018) LC–MS Challenges in Characterizing and Quantifying Monoclonal Antibodies (mAb) and Antibody-Drug Conjugates (ADC) in Biological Samples. *Curr Pharmacol Reports*, **4**: 45-63.2198-641X

Widdison W, Wilhelm S, Veale K, Costoplus J, Jones G, Audette C, Leece B, Bartle L, Kovtun Y, and Chari R (2015) Metabolites of antibody-maytansinoid conjugates: characteristics and in vitro potencies. *Mol Pharm* **12**:1762–1773.

Xu K, Liu L, Saad OM, Baudys J, Williams L, Leipold D, Shen B, Raab H, Junutula JR, Kim A, et al. (2011) Characterization of intact antibody-drug conjugates from plasma/serum in vivo by affinity capture capillary liquid chromatography-mass spectrometry. *Anal Biochem* **412**:56–66.

Yu SF, Zheng B, Go M, Lau J, Spencer S, Raab H, Soriano R, Jhunjhunwala S, Cohen R, Caruso M, et al. (2015) A novel anti-CD22 anthracycline-based antibody-drug conjugate (ADC) that overcomes resistance to auristatin-based ADCs. *Clin Cancer Res* **21**:3298–3306.

Zhang D, Hop CE, Patilea-Vrana G, Gampa G, Seneviratne HK, Unadkat JD, Kenny JR, Nagapudi K, Di L, Zhou L, et al. (2019) Drug concentration asymmetry in tissues and plasma for small molecule-related therapeutic modalities. *Drug Metab Dispos* DOI: 10.1124/dmd.119.086744 [published ahead of print].

Zhang D, Pillow TH, Ma Y, Cruz-Chuh JD, Kozak KR, Sadowsky JD, Lewis Phillips GD, Guo J, Darwish M, Fan P, et al. (2016a) Linker immolation determines cell killing activity of disulfide-linked pyrrolobenzodiazepine antibody-drug conjugates. *ACS Med Chem Lett* **7**:988–993.

Zhang D, Yu SF, Khojasteh SC, Ma Y, Pillow TH, Sadowsky JD, Su D, Kozak KR, Xu K, Polson AG, et al. (2018) Intratumoral payload concentration correlates with the activity of antibody-drug conjugates. *Mol Cancer Ther* **17**:677–685.

Zhang D, Yu SF, Ma Y, Xu K, Dragovich PS, Pillow TH, Liu L, Del Rosario G, He J, Pei Z, et al. (2016b) Chemical structure and concentration of intratumor catabolites determine efficacy of antibody drug conjugates. *Drug Metab Dispos* **44**:1517–1523.

Address correspondence to: Dr. Donglu Zhang, Genentech, 1 DNA Way, South San Francisco, CA 94080. E-mail: zhang.donglu@gene.com; or Dr. Cornelis E.C.A. Hop, Genentech, 1 DNA Way, South San Francisco, CA 94080. E-mail: hop.cornelis@gene.com

Downloaded from dmd.aspetjournals.org at ASPET Journals on April 18, 2024

Supplemental

Exposure-Efficacy Analysis of Antibody-Drug Conjugates Delivering an Excessive Level of Payload to Tissues

Donglu Zhang, Peter S Dragovich, Shang-Fan Yu, Yong Ma, Thomas H Pillow, Jack D Sadowsky, Dian Su, Wei Wang, Andrew Polson, S Cyrus Khojasteh, Cornelis ECA Hop

Affiliation: Drug Metabolism & Pharmacokinetics (DZ, YM, SCK, DS, WW, CECAH), Discovery Chemistry (THP, PSD), Translational Oncology (SY, AP), Protein Chemistry (JDS), Genentech, South San Francisco, CA 94080, USA.

Supplemental contains:

Table S1. Quantitation of MMAE, and DMx (DM1, DM3, and DM4) and associated methylated metabolites (methylated DMx, DM-Me) in tumors of xenograft mice following intravenously administration of corresponding ADC conjugates

Table S2. Quantitation of total antibody (Tab) in plasma of xenograft mice following intravenously administration of corresponding ADC conjugates

Figure S1. Correlation (X-Y plots) of tumor growth inhibition with intratumor DMx (DM+DM-Me) in mice bearing human CD22-expressing BJAB.Luc xenografts

Figure S2. Body weights from *In vivo* efficacy studies of PBD-, MMAE-, and DMx-ADCs in mice bearing human HER2-expressing Fo5 or human CD22-expressing BJAB.Luc xenografts (n = 8) after intravenous administration of corresponding ADCs A1-A4 (I), B1-B4 (II), C1-C8 (III), and D1-3 (IV, V, VI)

Figure S3. Correlation analysis of tumor growth inhibition with intratumor MMAE concentrations from Conjugates B1-B4 in mice bearing human CD22-expressing BJAB.Luc xenografts

Figure S4. Correlation analysis of tumor growth inhibition with intratumor DMx-Me concentrations from Conjugates C1-C8 in mice bearing human CD22-expressing BJAB.Luc xenografts

Table S1. Quantitation of MMAE and DMx (DM1, DM3, and DM4) and associated methylated metabolites (methylated DMx) in tumors of xenograft mice following intravenously administration of corresponding ADC conjugates

A

Conjugate	ADC name	MMAE Concentrations (nM) at Day 4
		Day 4
B1_1	CD22-Me-SS-MMAE	3.30±0.9
B1	CD22-Me-SS-MMAE	19.1±0.1
B2	CD22-Me-SS-PAB-MMAE	87.1±8.3
B3	CD22-DiMe-SS-MMAE	42.1±1.2
B4	CD22-Val-Cit-PAB-MMAE	55.6±13.3

B

Conjugate	ADC name	DMx Concentrations (nM) at Day 21	
		Day 21	
		Methylated DMx	DMx thiol
C1	CD22-SS-DM1	2.5±0.6	68.4±11.2
C2	CD22-SS-DM3	43.4±14.6	24.8±3.1
C3	CD22-MPEO-DM1	<LLOQ	7.3±1.9
C4	CD22-SPDB-DM4	5.4±2.9	<LLOQ
C5	CD22-MBT-DM4	3.4±0.6	<LLOQ
C6	CD22-SS-DM4	53.6±16.0	15.0±0.0
C7	CD22-Fc-SS-DM4	13.5±2.9	7.8±1.8
C8	CD22-Fc-SS-DM3	4.3±1.9	<LLOQ

Table S2. Quantitation of total antibody (Tab) in plasma of xenograft mice following intravenously administration of corresponding ADC conjugates in mice bearing human human CD22-expressing BJAB.Luc xenografts

A

Conjugate	ADC name	Tab (μg/mL)			$AUC_{0\text{-}7\ day}$
		Day 1	Day 4	Day 7	μg/mL●day
B1	CD22-Me-SS-MMAE	229±11.3	312±10.2	232±7.59	1746±404
B2	CD22-Me-SS-PAB-MMAE	193±10.2	140±56.8	125±107	1072±226
B3	CD22-DiMe-SS-MMAE	134±17.8	122±2.57	115±21.6	809±176
B4	CD22-Val-Cit-PAB-MMAE	10.8±2.57	5.87±1.20	6.30±2.35	49.0±10.0

B

Conjugate	ADC name	Tab (μg/mL)			$AUC_{0\text{-}7\ day}$
		Day 1	Day 3	Day 7	μg/mL●day
C1	CD22-SS-DM1	13.9±3.02	15.4±0.47	11.2±0.06	103±167
C2	CD22-SS-DM3	11.7±0.28	14.6±1.56	11.7±1.65	95.7±17.9
C3	CD22-MPEO-DM1	15.5±3.30	14.0±2.50	12.1±1.00	107±15.9
C4	CD22-SPDB-DM4	7.91±0.31	6.63±0.59	4.63±0.45	48.9±5.54
C5	CD22-MBT-DM4	13.1±0.21	10.9±0.07	6.80±0.34	79.1±8.20
C6	CD22-SS-DM4	13.9±0.32	13.5±0.56	8.86±0.78	93.1±12.3
C7	CD22-Fc-SS-DM4	15.6±0.30	11.7±1.13	13.1±0.54	100±14.1
C8	CD22-Fc-SS-DM3	13.8±0.28	10.7±0.60	10.1±0.21	86.4±11.0

Figure S1. Correlation (X-Y plots) of tumor growth inhibition with intratumor concentrations of DMx and methylated DMx in mice bearing human CD22-expressing BJAB.Luc xenografts

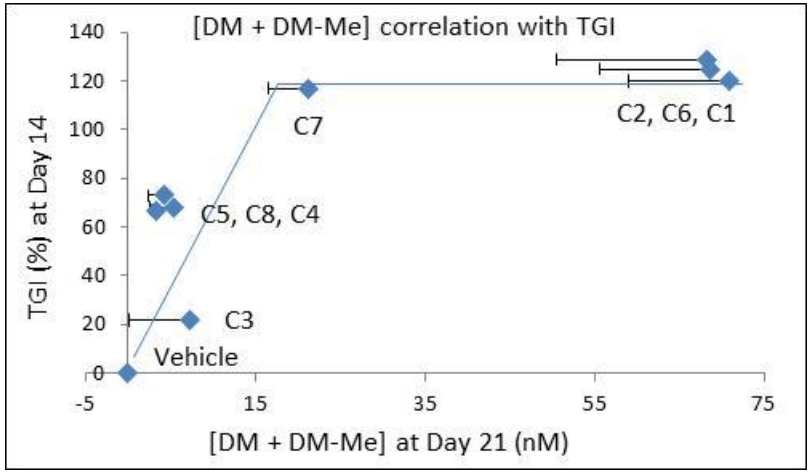

Figure S2. Body weights from *In vivo* efficacy studies of PBD-, MMAE-, and DMx-ADCs in mice bearing human HER2-expressing Fo5 or human CD22-expressing BJAB.Luc xenografts (n = 8) after intravenous administration of corresponding ADCs A1-A4 (I), B1-B4 (II), C1-C8 (III, and D1-3 (IV, V, VI).

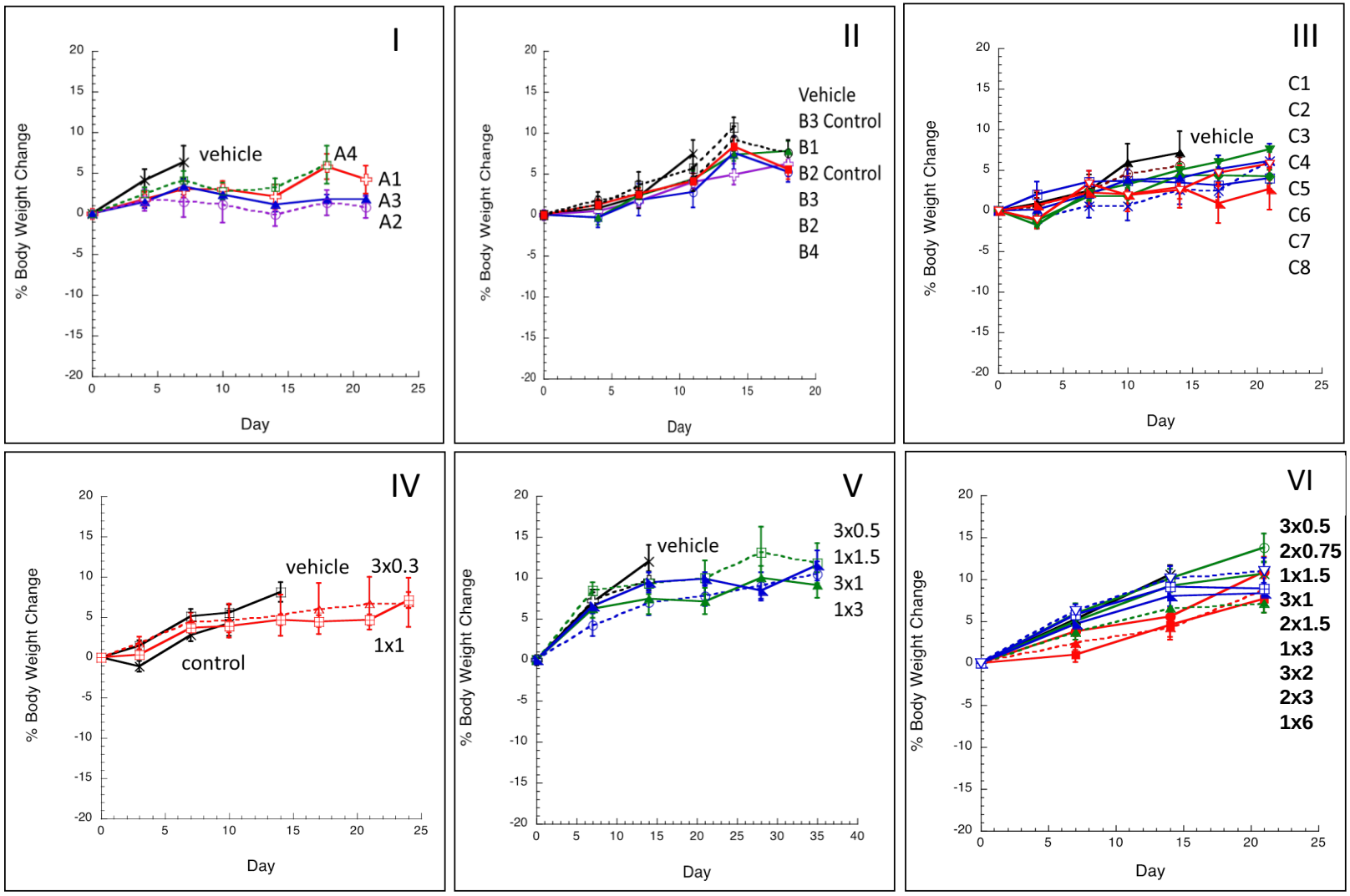

Figure S3. Correlation analysis of tumor growth inhibition with intratumor MMAE concentrations from Conjugates B1-B4 in mice bearing human CD22-expressing BJAB.Luc xenografts

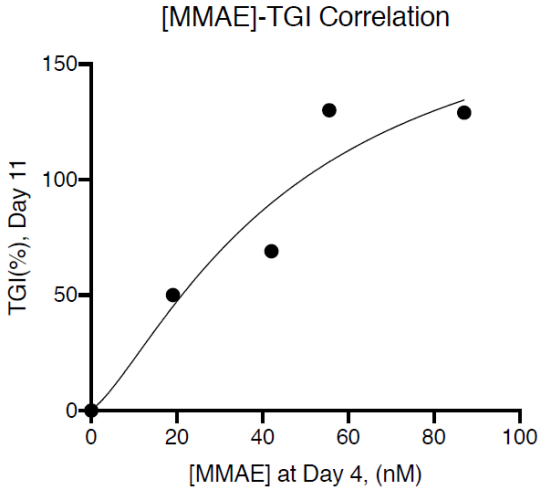

[Agonist] vs. response -- Variable slope (four parameters)	
Best-fit values	
Bottom	0.7400
Hillslope	1.339
Top	192.8
EC50	46.87
logEC50	1.671
Span	192.1
95% CI (profile likelihood)	
Bottom	-399.2 to 247.7
Hillslope	???
Top	-102.5 to 746.3
EC50	???
logEC50	
Goodness of Fit	
Degrees of Freedom	1
R squared	0.9192
Sum of Squares	987.4
Sy.x	31.42
Constraints	
EC50	EC50 > 0
Number of points	
# of X values	5
# Y values analyzed	5

Figure S4. Correlation analysis of tumor growth inhibition with intratumor DMx-Me concentrations from Conjugates C1-C8 in mice bearing human CD22-expressing BJAB.Luc xenografts

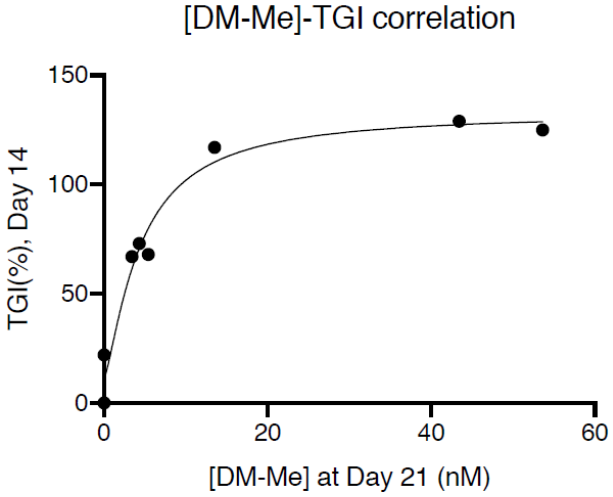

[Agonist] vs. response -- Variable slope (four parameters)	
Best-fit values	
Bottom	11.28
Hillslope	1.326
Top	133.2
EC50	4.469
logEC50	0.6502
Span	121.9
95% CI (profile likelihood)	
Bottom	-10.33 to 32.95
Hillslope	0.3842 to 4.068
Top	108.3 to ???
EC50	1.867 to ???
logEC50	0.2712 to ???
Goodness of Fit	
Degrees of Freedom	4
R squared	0.9694
Sum of Squares	481.7
Sy.x	10.97
Constraints	
EC50	EC50 > 0
Number of points	
# of X values	8
# Y values analyzed	8